ELSEVIER

Microelectronics Reliability 43 (2003) 2055–2064

MICROELECTRONICS RELIABILITY

www.elsevier.com/locate/microrel

The study on failure mechanisms of bond pad metal peeling: Part B—Numerical analysis

Insu Jeon *

PKG & Module R&D Center, Hynix Semiconductor Inc., San 136-1, Ami-ri, Bubal-eub, Ichon-si, Kyoungki-do 467-791, South Korea

Received 27 January 2003; received in revised form 15 June 2003

Abstract

According to the results of Part A of this paper [Microelectron. Reliab., this issue], the vertical tension loading transferred from the capillary is clarified as the direct driving force for bond pad metal peeling. Furthermore, the crack on the bonding pad is identified as the direct cause of the pad peeling. However, the major driving force for the crack that is correlated to the four main loadings described in the part A of this paper is not clarified. In order to find the driving force for the crack, whole ball bonding process of ultrasonic wire bonding is simulated by finite element method. The results of this study indicate that the horizontal vibration of the capillary controlled by ultrasonic power of the bonding machine has the most serious effect on the crack on the bonding pad as well as its propagation into the oxide layers in SDRAM chip. Thus it can be the major driving force for the crack.
© 2003 Elsevier Ltd. All rights reserved.

1. Introduction

Bond pad metal peeling [1–3] which is recognized as a serious bond ability and ball bond reliability problem in electronic packaging industry is analyzed with experimental investigation in Part A of this study [1]. According to the results of the study, the vertical tension loading transferred from the capillary is clarified as the direct driving force of the pad peeling and the crack on the bonding pad as well as its propagation into the oxide layers is identified as the direct cause of the pad peeling. However, the major driving force for the crack that is correlated to the four main loadings described in the paper [1] is not clarified. These four loadings are strongly affected by bonding parameters because these parameters, which can be adjustable in the bonding machine, control the behavior of the capillary and the heater block temperature during ultrasonic wire bonding. There are four main bonding parameters in ultrasonic wire bonding: bonding force, bonding time, heater block temperature and ultrasonic power.

Many researchers investigated the effects of those parameters on wire bonding. Guzmann and Mahaney [4] and Hu et al. [5] found that the ultrasonic power is a dominant variable in ball formation and has a critical effect on the bond shear strength. Liang et al. [6] and Shu [7] made a lot of efforts to optimize the bonding parameters in order to improve the bondability characterized by the ball shear stress and the ball bond reliability determined by in situ ball bond degradation measurement. Particularly, Liang et al. [6] introduced a concept of 'reduced bonding parameter' and they were able to relate the bonding parameters directly to bond ability and ball bond reliability.

Several numerical analyses of wire bonding process have been carried out for understanding the bonding mechanism. Among these works, Chidambaram [8] evaluated gold wire fatigue parameters and 'mean time to failure' using temperature cycle data in conjunction with the strains obtained from finite element analysis. Moreover, Takahasi et al. [9] simulated wire deformation processes during thermo-compression bonding without ultrasonic vibration using finite element

* Department of Mechanical and Control Engineering, Tokyo Institute of Technology, Ishikawadai 1-204, 2-12-1, O-okayama, Meguro-ku, Tokyo 152-8552, Japan. Tel.: +81-3-5734-2783; fax: +81-3-5734-3917.

E-mail address: i_jeon@ichizai-7.mep.titech.ac.jp (I. Jeon).

0026-2714/$ - see front matter © 2003 Elsevier Ltd. All rights reserved.
doi:10.1016/S0026-2714(03)00213-0

technique. The finite element simulation of the wire looping process in ball-wedge wire bonding was performed by Tay et al. [10]. They compared the obtained resultant wire bonding profiles with actual samples. Recently, Takahasi et al. [11,12] published two papers about numerical analysis of fine lead bonding. They reported the effect of pad thickness and pad mechanical properties on inner lead bonding considering the visco-plastic behavior of lead and pad.

In this paper, the whole ball bonding process of ultrasonic wire bonding is simulated by finite element method considering the bonding parameters which are adjusted for the actual wire bonding process to find the driving force for the crack on the bonding pad and its propagation into the oxide layers. Under the assumption of elastic–plastic behavior of the bonding pad and elastic behavior of the oxide layers, occurrence of the crack is predicted by the maximum equivalent plastic strain in the bonding pad and the maximum Mises stress in the oxide layers.

2. Characterization of ultrasonic wire bonding problem

The ultrasonic wire bonding has various complex problems, such as dynamic load transfer, diffusion between Au ball and Al bonding pad, mechanical and thermal contact, friction and transient heat transfer problem. In this study, however, the dynamic behavior of the capillary and the ball is replaced with the behavior without mass effect because the deformation of the capillary itself is not important and the mass of the ball is very small. Furthermore, for the sake of simplicity in numerical analysis, the chemical reaction, namely, diffusion Al bonding pad and Au ball (air free ball) is ignored.

In order to compensate the bonding strength between the ball and the bonding pad during the ultrasonic wire bonding, the frictional contact problem for these materials is considered. In addition, the thermal contact and the transient heat transfer problem are considered for the numerical calculation.

3. Governing equations for mechanical contact problem

Consider two bodies that are contacting mechanically and thermally with each other under plane strain deformation shown in Fig. 1. It is assumed that the material property of two bodies is isotropic and each of two bodies contains five types of boundary condition. The displacement and the traction boundary conditions are prescribed in Γ_u and Γ_t, respectively. The temperature

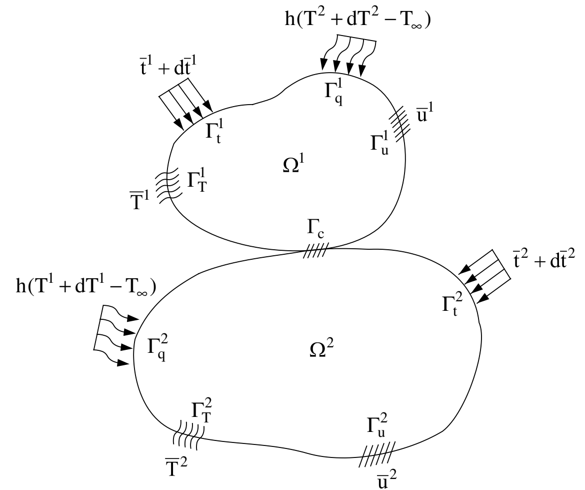

Fig. 1. Two bodies in contact with the mechanical and the thermal boundary condition.

and the convection boundary conditions are given in Γ_T and Γ_q, respectively. Moreover, Γ_c denotes the part of boundary where contacts may occur.

Then in the absence of the body forces the equilibrium equation is written as

$$(\sigma_{ij} + \mathrm{d}\sigma_{ij})^k_{,j} = 0 \quad \text{in } \Omega^k \tag{1}$$

where superscript 'k' denotes body numbering and the comma indicates partial differentiation with respect to the Cartesian coordinate x_i. When the loading applied on the boundary increases, the plastic deformation will occur. Under the plastic loading, the incremental form of the constitutive equations for thermal elastic–plastic material [13–15] can be written as

$$\mathrm{d}\sigma_{ij} = 2G\left(\mathrm{d}\varepsilon_{ij} + \frac{v}{1-2v}\delta_{ij}\,\mathrm{d}\varepsilon_{ll}\right) - \frac{3Gs_{kl}\,\mathrm{d}\varepsilon_{kl}s_{ij}}{\sigma_e^2(1+H/3G)} + \frac{(\partial\sigma_Y/\partial T)\mathrm{d}T}{\sigma_e(1+H/3G)}s_{ij} - 2K\delta_{ij}\,\mathrm{d}\varepsilon^T \tag{2}$$

Under the elastic loading or unloading, the change in stress $\mathrm{d}\sigma_{ij}$ can be written as

$$\mathrm{d}\sigma_{ij} = 2G\left(\mathrm{d}\varepsilon_{ij} + \frac{v}{1-2v}\delta_{ij}\,\mathrm{d}\varepsilon_{ll}\right) - 2K\delta_{ij}\,\mathrm{d}\varepsilon^T \tag{3}$$

where T is the temperature, G is the shear modulus, v is the Poisson's ratio and K is the bulk modulus of the material. Moreover, $H = \partial\sigma_Y/\partial\varepsilon^p$ is the hardening modulus, σ_Y is the yield stress, s_{ij} is the stress deviator, σ_e is the effective stress and ε^T is the uniaxial thermal dilatation for the material. For the concise expression of Eqs. (2) and (3), the superscript 'k' which refers the body numbering is omitted.

The strain-displacement relation is

$$\mathrm{d}\varepsilon_{ij} = \tfrac{1}{2}(\mathrm{d}u_{i,j} + \mathrm{d}u_{j,i}) \tag{4}$$

The mechanical boundary conditions are given as follows:

$$u_i = \bar{u}_i \quad \text{on } \Gamma_u^k \tag{5}$$

$$(\sigma_{ij} + \mathrm{d}\sigma_{ij})^k n_j^k = \bar{t}_i^k + \mathrm{d}\bar{t}_i^k \quad \text{on } \Gamma_t^k \tag{6}$$

where $\bar{u}_i$, n_j and $\bar{t}_i$ are the prescribed displacement, the unit normal vector and the traction on each boundary, respectively.

The mechanical contact conditions can be represented as

$$p = 0 \quad \text{on } \Gamma_\mathrm{c} \tag{7}$$

$$f_1 \leqslant 0, \; f_2 \leqslant \mu f_1 \quad \text{on } \Gamma_\mathrm{c} \tag{8}$$

For the contact boundary, the penetration between each body is denoted by p. Therefore, $p = 0$ means the non-penetration condition for the contact problem. The contact traction component and the friction coefficient are denoted by f_i and μ, respectively.

4. Governing equations for thermal contact problem

In Fig. 1, the heat of each body is transferred to the atmosphere through the boundary Γ_q and is exchanged with each other through the boundary Γ_c depending on time. The heat transfer in transient state has to be considered in this case. The governing equations for the transient heat transfer can be written as

$$(q_i + \mathrm{d}q_i)^k_{,i} = \rho^k c_p^k \frac{\partial (T + \mathrm{d}T)}{\partial t} \quad \text{in } \Omega^k \tag{9}$$

$$\mathrm{d}q_i^k = -\kappa^k T_{,i} \tag{10}$$

where ρ is the density, c_p is the specific heat, κ is the coefficient of thermal conductivity, the q_i is the heat flux component and $\mathrm{d}T$ is the temperature change during a load increment.

The initial boundary condition is

$$T|_{t=0} = T_0 \tag{11}$$

The thermal boundary conditions are given as

$$(q_i + \mathrm{d}q_i)^k n_i^k = h[(T + \mathrm{d}T) - T_\infty] \quad \text{on } \Gamma_q^k \tag{12}$$

$$T = \bar{T} \quad \text{on } \Gamma_T^k \tag{13}$$

where T_0 is the initial temperature of each body, $\bar{T}$ is the prescribed temperature on Γ_T, T_∞ is the temperature of the atmosphere and h is the convection coefficient.

The thermal contact condition can be expressed as follows:

$$(q_i + \mathrm{d}q_i)^k n_i^k = h_\mathrm{c}[(T_i + \mathrm{d}T_i)_\mathrm{b} - (T_j + \mathrm{d}T_j)_\mathrm{b}] \quad \text{on } \Gamma_\mathrm{c} \tag{14}$$

here T_i and T_j are the temperatures of two bodies contacted with each other. The subscript 'b' represents the boundary of contact surface. Moreover h_c is the thermal contact conductance, which is divided into three terms as follows [16,17]:

$$h_\mathrm{c} = h_\mathrm{cs} + h_\mathrm{cm} + h_\mathrm{cr} \tag{15}$$

where h_cs, h_cm and h_cr are the conductance components of solid, fluid medium and radiation, respectively. The expressions of each component will be shown in Appendix A.

5. Finite element formulation

The finite element formulation for the mechanical contact problem can be obtained using Eqs. (1)–(8) and the principle of virtual work, which can be written as

$$\int_V (\sigma_{ij} + \mathrm{d}\sigma_{ij})_{,j} \delta \mathrm{d}u_i \, \mathrm{d}V = 0 \tag{16}$$

For the case of the thermal contact problem, Eqs. (9)–(15) and the variational equation for transient heat transfer equation (17) can be utilized.

$$\int_V \left[(q_i + \mathrm{d}q_i)_{,i} - \rho c_p \frac{\partial (T + \mathrm{d}T)}{\partial t} \right] \delta \mathrm{d}T \, \mathrm{d}V = 0 \tag{17}$$

After obtaining the matrix equations for finite element formulation from Eqs. (16) and (17), these two matrix equations are combined with each other to find the mechanical and thermal solutions, simultaneously. For more detailed procedure of the formulation, see the work of Park and Kwak [18]. In this study, however, the package code ABAQUS is used for these solutions because ABAQUS can offer the penalty method or the Lagrangian multiplier method for the mechanical contact problem and can support the analysis technique to solve the thermal contact problem.

6. Material properties for numerical analysis

The capillary and the wire for ultrasonic wire bonding are usually made from Al_2O_3 and 99.9% Au. The components of SDRAM chip such as the bonding pad, the oxide layers and the active die are also made from Al, SiO_2 species and Si, respectively. For numerical analysis, the representative material properties of those materials depending upon temperature are chosen from the material handbooks [19–21]. However, the

Table 1
The measured elastic modulus and the yield stress of the Au wire

Elastic modulus (GPa)	Yield stress (MPa)	Temperature (K)
73.65775	191.6	Room temperature
73.45181	181.923	323.15
72.43192	168.38	373.15
69.41147	160.635	423.15
66.54793	156.764	473.15
59.02623	141.28	523.15

elastic modulus and the yield stress depending on the temperature of the Al thin film are selected from the paper of Shi and Tu [22] and those of the Au wire are taken from the measured data in Table 1.

For the elastic–plastic calculation based on the incremental plasticity (2) and (3) is processed with a power-law hardening rule of the form [13,14]

$$\frac{\bar{\varepsilon}^p}{\varepsilon_Y} = \alpha\left(\frac{\bar{\sigma}}{\sigma_Y}\right)^m \tag{18}$$

where $\bar{\varepsilon}^p$ is the equivalent plastic strain, $\varepsilon_Y = \sigma_Y/E$ is a reference strain component; $\bar{\sigma}$ is the Mises stress, α is the non-dimensional parameter, m is the power-law hardening exponent, typically $m = 1$ is the linear elastic and $m = \infty$ is the perfectly plastic. We choose $\alpha = 1$ and $m = 12$ for numerical computation.

7. Finite element meshes and initial boundary conditions

The finite element meshes for the capillary, the wire and the air free ball are presented in Fig. 2. The inner diameter of the capillary tip is 28.74 μm and all of the other geometric data are taken from its design drawing. The diameter of the wire is 20.32 μm and the total length of the wire is chosen to be 1240 μm in order to save the computation time. The diameter of the ball, which is formed by EFO (electric flame off) electrode, is empirically known as 2.5–3 times that of the wire, thus it is set to be 60.96 μm. The mesh structure of SDRAM chip is shown in Fig. 3. The geometric data of the chip components including the bonding pad and the various oxide layers are taken from the measured data of a real chip. The isoparametric plane strain element with eight nodes is adopted for modeling. The selective reduced integration scheme is chosen to prevent the excessive incompressible constraint in elastic–plastic deformations.

For the initial temperature boundary condition, the room temperature, 278.15 K is selected for the capillary and the chip, and the measured temperature, 1413.75 K is selected for the wire and the ball to consider the transient heat transfer during the ball bonding process of ultrasonic wire bonding.

8. Boundary conditions for mechanical solution

In the ball bonding process, x-direction degree of freedom of the nodes is fixed, namely, $u_1 = 0$ on the

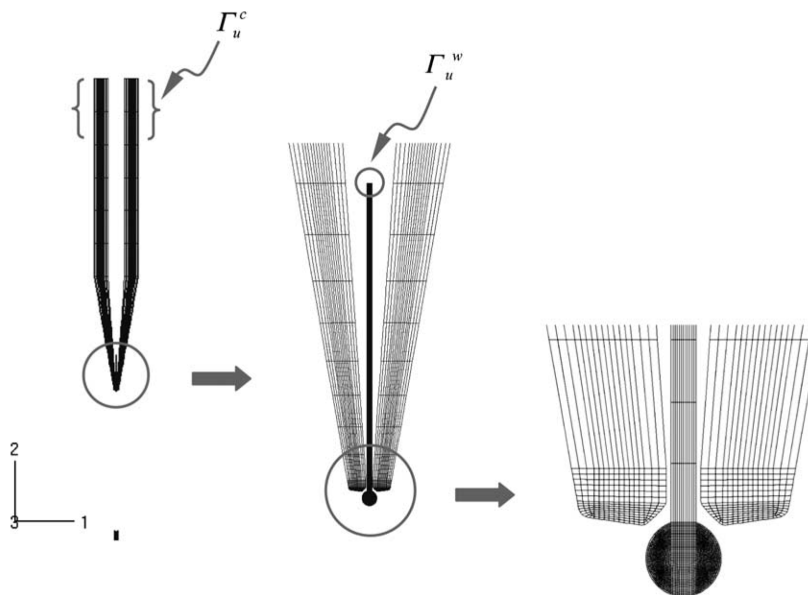

Fig. 2. The finite element mesh shape of the capillary, the wire and the ball.

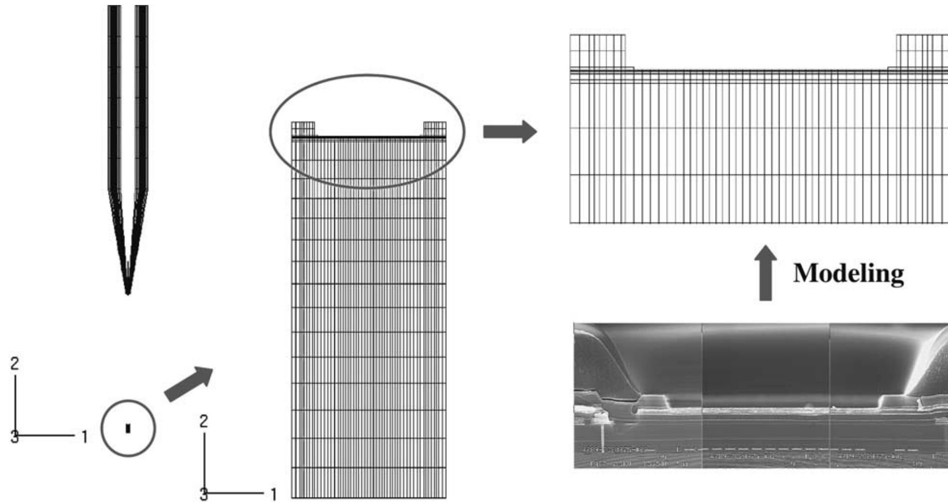

Fig. 3. The finite element mesh shape of the chip and the cross-section SEM image of a real chip.

outside of the capillary and on Γ_u^{w} (see Fig. 2) to prevent the rigid body motion of the wire and the ball. Furthermore the symmetry boundary condition is applied to the left and the right side of the chip and the y-direction degree of freedom of the nodes is fixed, namely, $u_2 = 0$, on the bottom of the chip.

Because the reasonable description of the behavior of a capillary during the ball bonding process as the displacement boundary condition is essential to the numerical analysis, it is divided into four types of behavior following the loading types of Jeon and Chung [1], such as the vertical descent, the vertical compression, the horizontal vibration and the vertical ascent.

For the vertical descent of the capillary, $u_2 = -5014.5$ μm and $u_2 = -5006.5$ μm is applied to the nodes on Γ_u^{c} and Γ_u^{w} (see Fig. 2), respectively, in 2.5 ms until the lower surface of the ball contacts with the bonding pad and the upper surface of the ball contacts with the tip of capillary, simultaneously. Note that the time of this process is decided from the 2 m/s velocity of the capillary. After then $u_2 = -21.7$ μm, which means the 50 gf of bonding force, is added to the nodes on Γ_u^{c} and $u_2 = -5006.5$ μm on Γ_u^{w} is removed for the vertical compression of the capillary during 30 ms. However, $u_1 = 0$ on the outside of the capillary is still remaining in this stage. After the vertical compression, the x-direction displacement is applied for the horizontal vibration of the capillary on the outside of the capillary but $u_2 = -21.7$ μm is still maintaining on Γ_u^{c}. The amplitude and the frequency of the vibration are chosen as $u_1 = 2$ μm, which means the 60 mW of the ultrasonic power, and 125 KHz of frequency fixed in the bonding machine, respectively. To save the computation time, only 0.008 ms in accordance with 1 cycle of the vibration is applied to the capillary even though the actual bonding time of the capillary is about 5–15 ms. Finally, for the vertical ascent, $u_1 = 0$ and $u_2 = 29.7$ μm are applied to the nodes on the outside of the capillary and Γ_u^{c}, respectively, in 20 ms.

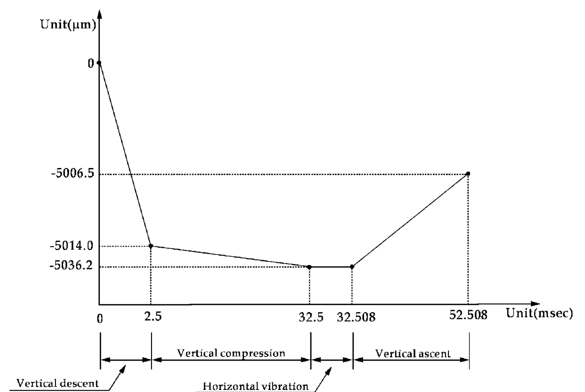

Fig. 4. The y-direction displacement loaded on Γ_u^{c} of the capillary according to the process time.

The whole y-direction displacement boundary condition loaded on Γ_u^{c} of the capillary according to the bonding process time is presented in Fig. 4. Note that all aforementioned values for the displacement boundary conditions and applied time are decided from the measured and empirically known data of actual ball bonding process of ultrasonic wire bonding.

9. Boundary conditions for thermal solution

Because of the fixed heater block temperature of the bonding machine, the bottom surface of the chip laid on the heater block always maintains constant temperature,

503.15 K during the ultrasonic wire bonding process. Therefore, the temperature boundary condition for the nodes on the bottom of the chip is prescribed to be 503.15 K.

The convection boundary condition is applied to the outside of the capillary, the whole surface of the ball and the top surface of the chip. The symmetry condition for the convection is also applied to the left and the right side of the chip. During the whole ball bonding process except the vertical descent process of the capillary and the ball, it is assumed that all surfaces of each body are exposed to the natural convection. Hence the convection coefficient is chosen as $h = 15$ W/m^2 K for those surfaces. During the vertical descent process, however, these coefficients are selected as $h = 635.9$ W/m^2 K for the surface of the ball and $h = 52.38$ W/m^2 K for the outside of the capillary because of their velocity.

In order to obtain these coefficients, a 1 m-long cylinder and a 1 m-wide plate are proposed for the surface of the ball and the outside of the capillary, respectively, along with the plane strain deformation assumption of this problem. Then the measured velocity of the capillary and the non-dimensional numbers, i.e., Nusselt number, Reynolds number and Prandtl number are utilized for calculation.

10. Numerical results and discussion

The deformation results for the whole ball bonding process are shown in Figs. 5 and 6. The status of the capillary after the vertical descent is presented in Fig. 5, which shows that the tip of the capillary contacts with the upper surface of the ball and the lower surface of the ball contacts with the bonding pad, simultaneously.

In Fig. 6, the deformed shapes of the ball and the bonding pad after each behavior of the capillary are shown. The ball is largely deformed during the vertical compression of the capillary and the shape around the ball neck is highly affected by the inner shape of the capillary tip in this stage. Furthermore, it is found that the bonding pad is experienced severe deformation by the deformed ball during the horizontal vibration because the shearing load induced by the capillary directly transmits to the bonding pad through the deformed ball. The x-direction displacement boundary condition applied to the outside of the capillary versus increasing time for the horizontal vibration is presented in Fig. 7.

Two deformed shapes of the ball obtained from the numerical analysis and the actual manufacturing process are presented in Fig. 8. Fig. 8(b) is the cross-section SEM image of the actually bonded ball. The same set of the bonding parameters is used for comparing their deformed shapes with each other. Even though there are some differences in the geometric data as well as the material data between the modeled and the actual ultrasonic wire bonding process, Fig. 8 shows a good agreement between these two shapes.

The temperature change of the ball and the bonding pad versus increasing time during ball bonding process is shown in Fig. 9. For obtaining those temperatures, two points from each body where the mechanical contact is initiated between the ball and the pad are selected. In Fig. 9, it is shown that the temperature of the ball is rapidly decreased during the vertical descent and the early stage of the vertical compression. Moreover, the heat of the ball increases the temperature of the bonding pad rapidly when the contact between each body begins. After then, the temperatures of the ball and the bonding pad go to same value and decrease together to the heater

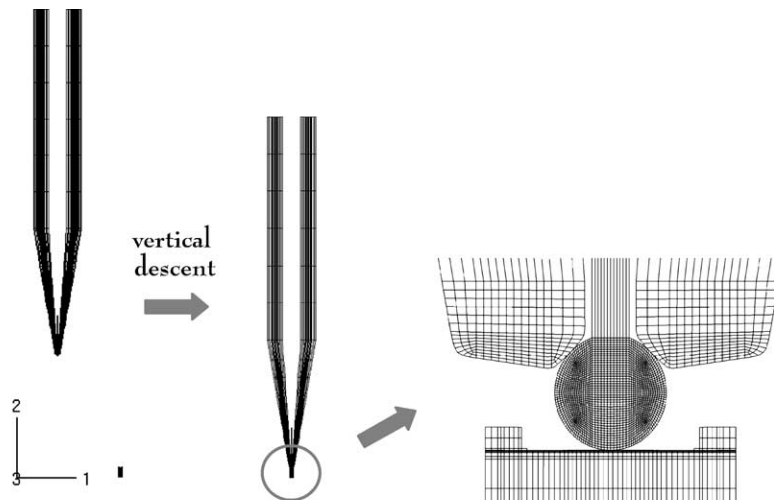

Fig. 5. The vertical descent of the capillary.

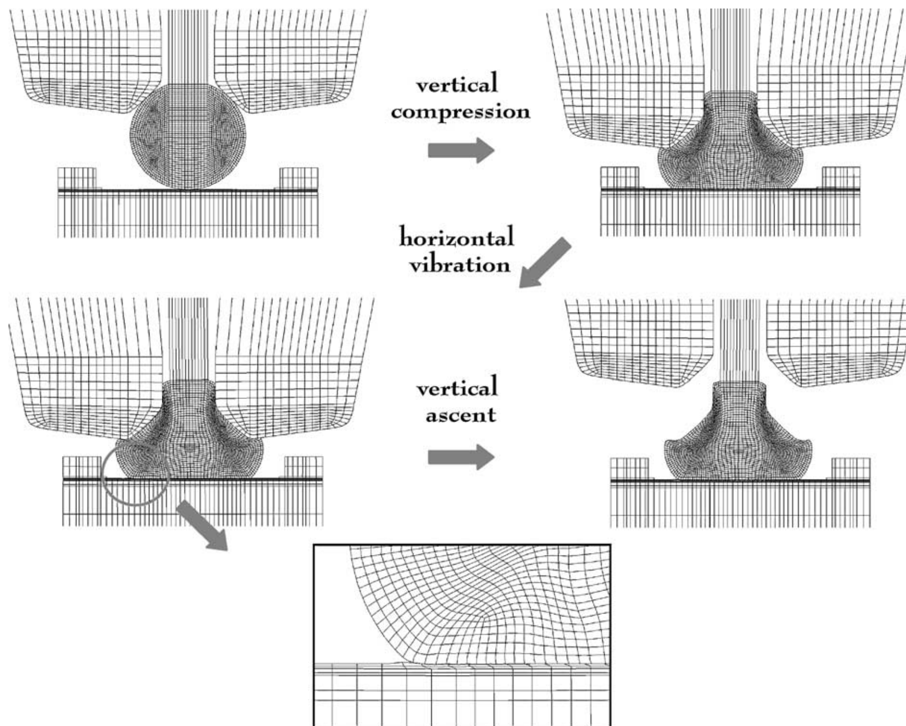

Fig. 6. The deformed shapes of the ball and the bonding pad during ball bonding process of ultrasonic wire bonding.

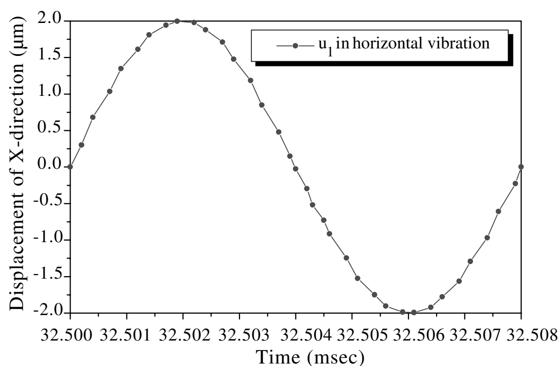

Fig. 7. The *x*-direction displacement of the capillary during the horizontal vibration.

block temperature. These results indicate that the temperature of the ball and the bonding pad is affected by the temperature of the heater block while the ball is deformed and vibrated.

Because of the severe deformation shape of the bonding pad during the horizontal vibration shown in Fig. 6, the equivalent plastic strain in the bonding pad and the Mises stress in the oxide layers underneath the pad during the whole ball bonding process are investigated. The changes of these values following the time of ball bonding process are shown in Figs. 10 and 11.

Fig. 10(a) and (b) show that the maximum value of equivalent plastic strain takes place in the bonding pad underneath the edge of the deformed ball ($x/L = 0.953$) during the horizontal vibration process which begins after 32.5 ms. Where 'L' means the length from the center to the edge of the interface between the deformed wire ball and the bonding pad before the vibration process and 'x' means an arbitrary position in the bonding pad from the center axis of the deformed wire ball. Because the equivalent plastic strain is closely related to the fracture of a ductile metal, the equivalent plastic strain in Fig. 10(a) and (b) explain that horizontal vibration has the most serious effect on the crack on the bonding pad underneath the edge of the deformed ball.

Fig. 11(a) and (b) show that the maximum value of Mises stress also takes place in the oxide layer beneath the edge of the deformed ball ($x/L = 1.047$), where 'x' means an arbitrary position in the oxide layer from the center axis of the deformed wire ball. Besides, it shows that the shearing load transferred during the horizontal vibration has more serious effect on the oxide layers than the compression load transferred during the vertical compression from 2.5 to 32.5 ms. Such Mises stress that mainly depends upon the horizontal vibration is

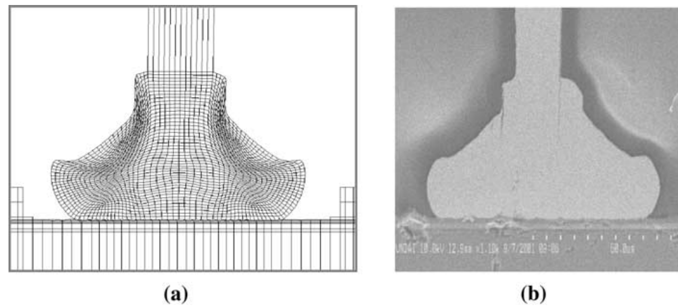

Fig. 8. The deformed shape of the ball obtained from (a) the numerical analysis and (b) the actual manufacturing process.

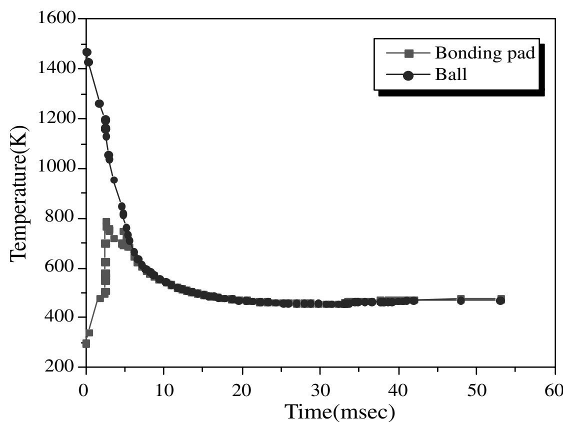

Fig. 9. The temperature of the ball and the bonding pad during ball bonding process.

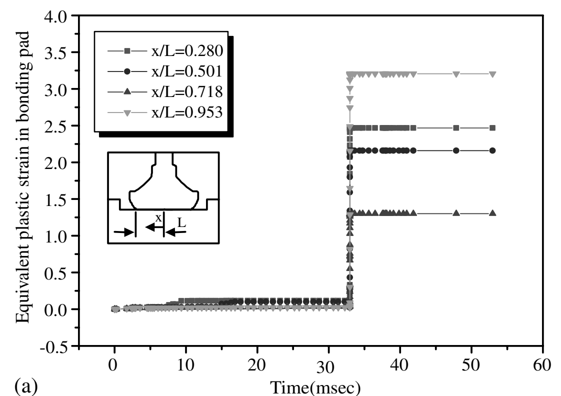

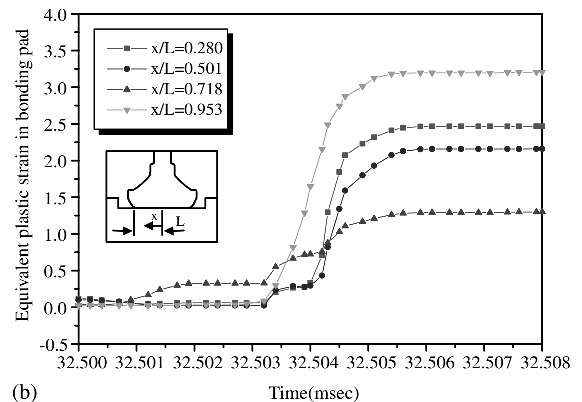

Fig. 10. The equivalent plastic strain in the bonding pad during (a) whole ball bonding process and (b) the horizontal vibration.

expected to make a significant effect on the fracture of the oxide layers and also to help the propagation of the crack on the pad into the oxide layers because the shearing load from the vibration can be the Mode I type loading for the crack on the bonding pad.

The role of the bonding time and the heater block temperature in ball bonding process also can be explained with the results of Figs. 10 and 11. The bonding time affects the accumulation of the equivalent plastic strain in the bonding pad and the Mises stress in the oxide layers during the horizontal vibration because the number of vibration cycles can be controlled by the bonding time. Moreover the heater block temperature affects the upward or downward shift of these values from current ones along the whole time of ball bonding process because the deformation and the vibration of the ball are mainly affected by this temperature (see Fig. 9).

Fig. 12(a) and (b) show the SEM images of the crack on the bonding pad obtained from the PCT (pad cratering test) after the regular ultrasonic wire bonding process and the fractured shape of the pad as well as the oxide layers obtained from the FIB works after the pad peeling, respectively (see [1]). These figures explain that the crack on the bonding pad is located around the edge of the deformed ball and the vertically fractured oxide layers is located under the cracked pad after the pad peeling. Therefore the actual occurring location of the crack on the bonding pad and the fractured oxide layers shows a good agreement with the location at which the maximum equivalent plastic strain and the maximum

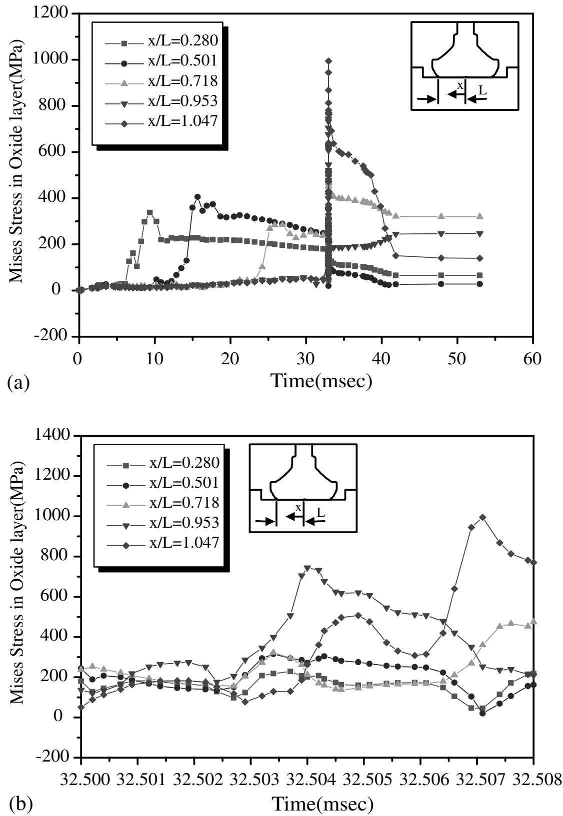

Fig. 11. The Mises stress in the oxide layer during (a) whole ball bonding process and (b) the horizontal vibration.

Mises stress are calculated from the numerical analysis presented in Figs. 10 and 11.

11. Concluding remarks

In order to find the major driving force for the crack on the bonding pad, whole ball bonding process of ultrasonic wire bonding is simulated by finite element method. According to the results of this study, the maximum equivalent plastic strain in the bonding pad and the maximum Mises stress in the oxide layers are calculated during the horizontal vibration process of the capillary. Furthermore, it is clarified that the horizontal vibration of the capillary controlled by ultrasonic power of the bonding machine has the most serious effects on the crack on the bonding pad as well as its propagation into the oxide layers. Thus it can be the major driving force for the crack. Therefore, careful decision of ultrasonic power of the bonding machine to control the horizontal vibration is essential to prevent the bond pad metal peeling of SDRAM chip.

Acknowledgements

I. Jeon thanks Dr. Jeong-Tak Moon of M.K. Electronic Co. Ltd. for supplying the experimental material properties of gold wire and Dr. Hyon-Jeong Lee for valuable advice. The electronic packaging engineers of Hynix Semiconductor Inc. is acknowledged for their technical supports and helpful discussions.

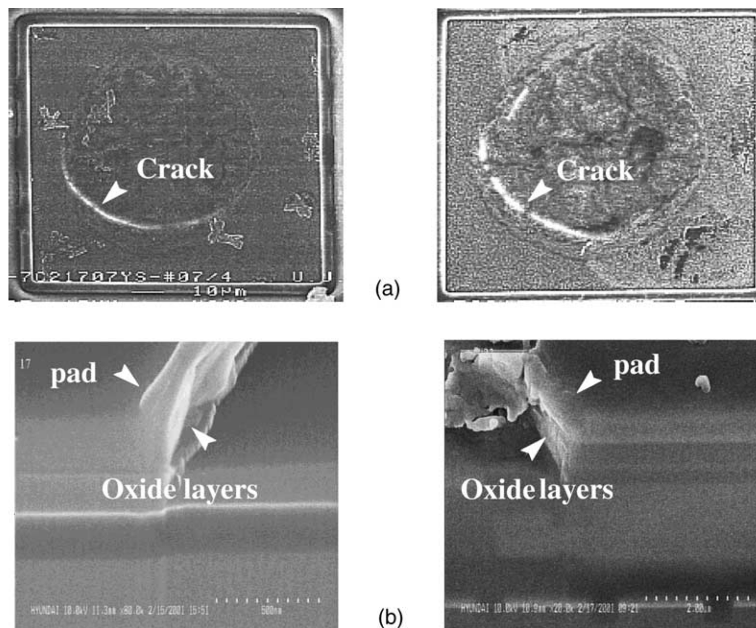

Fig. 12. SEM images of (a) the cracks on the bonding pads and (b) the fractured shapes of the oxide layers after the pad peeling.

Appendix A

For analyzing the thermal contact problem, the calculations of the thermal contact conductance, which is divided into solid, medium fluid and radiation contact conductance, are necessary (see [16,17]).

Firstly, the equation of solid contact conductance introduced by Mickic [23], which is obtained to account for contact interactions under plastic deformations is used for calculation:

$$h_{cs} = 3800 k_h R_a^{-0.257} [P/(M+P)]^{0.94} \quad (A.1)$$

where $k_h = 2k_i k_j/(k_i + k_j)$ and $R_a = \sqrt{(R_{ar} + R_{as})}$ are the mean thermal conductivity and arithmetic mean surface roughness, respectively. Furthermore, P is the contact pressure, and M is the hardness of the softer material.

Secondly, for the calculation of the medium fluid conductance, the equation achieved by Madhusudona and Fletcher [24] is selected:

$$h_{cm} = k_m/\delta_m \quad (A.2)$$

where k_m is the thermal conductivity of the medium and δ_m is the distance between two materials.

Finally, the equation obtained by Wong [25] for the radiation contact conductance is chosen:

$$h_{cr} = \sigma'[\varepsilon_i \varepsilon_j/(\varepsilon_i + \varepsilon_j - \varepsilon_i \varepsilon_j)] \times [(T_i^4|_b - T_j^4|_b)/(T_i|_b - T_j|_b)] \quad (A.3)$$

where σ' is the Stefan–Boltzmann constant, ε_i is the emissivity of the ith material, T is temperature at absolute scale and the subscript 'b' represents the boundary of contact surface.

Note that all of the aforementioned thermal contact conductances have been calculated for this study with the measured and empirically known data of each material used in ultrasonic wire bonding.

References

[1] Jeon I, Chung Q. The study on failure mechanisms of bond pad metal peeling: Part A—Experimental investigation. Microelectron Reliab, this issue [doi:10.1016/S0026-2714(03)00212-9].

[2] Tan CM, Er E, Hua Y, Chai V. Failure analysis of bond pad metal peeling using FIB and AFM. IEEE Trans Compon Pack Manuf Technol Part A 1998;21(4):585–91.

[3] Tan CM, Linggajaya K, Er E, Chai V. Effect of BOE etching time on wire bonding quality. IEEE Trans Compon Pack Technol 1999;22(4):551–7.

[4] Guzmann MS, Mahaney M. The bond shear test and application for the reduction of common causes of gold ball bond process variation. In: Reliability Physics Symposium 1992, 30th Annual Proceedings, International, 1992. p. 251–7.

[5] Hu SJ, Lim GE, Foong KP. Study of temperature parameters on the thermosonic gold wire bonding of high-speed CMOS. IEEE Trans Compon Hybrids Manu Technol 1991;14(4):855–8.

[6] Liang ZN, Kuper FG, Chen MS. A concept to relate wire bonding parameters to bondability and ball bond reliability. Microelectron Reliab 1998;38:1287–91.

[7] Shu WK. Fine pitch wire bonding development using statistical design of experiment. In: IEEE 1995 Proceedings, 45th Electronic Components and Technology Conference, 1995. p. 91–101.

[8] Chidambaram NV. A numerical and experimental study of temperature cycle wire bond failure. Electronic Components and Technology Conference 1991, 41st Annual Proceedings, 1991. p. 877–82.

[9] Takahasi Y, Shibamoto S, Inoue K. Numerical analysis of the interfacial contact process in wire thermocompression bonding. IEEE Trans Compon Pack Manuf Technol Part A 1996;19:213–23.

[10] Tay AAO, Seah BC, Ong SH. Finite element simulation of wire looping during wirebonding. Proc Adv Electron Pack 1997;1:399–406.

[11] Takahasi Y, Inoe M, Inoue K. Numerical analysis of fine lead bonding—effect of pad thickness on interfacial deformation. IEEE Trans Compon Pack Technol 1999;22:291–8.

[12] Takahasi Y, Inoe M, Inoue K. Numerical analysis of fine lead bonding—effect of pad mecanical properties on interfacial deformation. IEEE Trans Compon Pack Technol 1999;22:558–66.

[13] Mcmeeking RM. Finite-element formulations for problems of large elastic–plastic deformation. Int J Solids Struct 1975;11:601–16.

[14] Jeon I, Im S. The role of higher order eigenfields in elastic–plastic cracks. J Mech Phys Solids 2001;49:2789–818.

[15] Hetnarski RB. Thermal stress I. Netherlands: Elsevier Science Publishers BV; 1986. p. 300–89.

[16] Tseng AA. Thermal modeling of roll and strip interface in rolling processes: Part 1—Review. Numer Heat Transfer, Part A 1999;35:115–33.

[17] Tseng AA. Thermal modeling of roll and strip interface in rolling processes: Part 2—Simulation. Numer Heat Transfer, Part A 1999;35:135–54.

[18] Park J, Kwak B. Formulation of thermo-mechanical frictional contact based on complementary relations. Int J Solids Struct 1994;31:3217–31.

[19] Shackelford JF et al. CRC materials science and engineering handbook. CRC Press; 1994.

[20] Miner DF, Seastone JB. Handbook of engineering materials. New York: Wiley; 1955.

[21] Minges ML. Electronic materials handbook. ASM International; 1989.

[22] Shi LT, Tu KN. Finite element stress analysis of failure mechanisms in a multilevel metallization structure. J Appl Phys 1995;77:3037–41.

[23] Mickic BB. Thermal contact conductance; Theoretical considerations. Int J Heat Mass Transfer 1974;17:205–14.

[24] Madhusudana CV, Fletcher LS. Contact heat transfer—the last decade. AIAA J 1986;24:510–23.

[25] Wong HY. A survey of the thermal conductance of metallic conditions. ARC Report CP No. 973, London: Her Majesty's Stationery Office; 1968.